Supplementary Material - Anomalous Residual Surface Conductivity in A Superconductor with Strong Spin-Orbit Coupling

J. R. Chamorro[1,2,+], P. Chauhan[2,+], C. Sun[2], N. Varnava[2,3], M. J. Winiarski[4], N. Ng[1,2], H. K. Vivanco[1,2], L. A. Pressley[1,2], C. M. Pasco[1,2], D. Vanderbilt[2,3], Yi Li[2], N. P. Armitage[2], and T. M. McQueen[1,2,5,*]

[1]Department of Chemistry, The Johns Hopkins University, Baltimore, MD 21218, USA
[2]Institute for Quantum Matter, Department of Physics and Astronomy, The Johns Hopkins University, Baltimore, MD 21218, USA
[3]Department of Physics & Astronomy, Rutgers University, Piscataway, NJ 08854, USA
[4]Faculty of Applied Physics and Mathematics and Advanced Materials Center, Gdansk University of Technology, ul. Narutowicza 11/12, 80-233 Gdansk, Poland
[5]Department of Materials Science and Engineering, The Johns Hopkins University, Baltimore, MD 21218, USA
[*]mcqueen@jhu.edu
[+]these authors contributed equally to this work

Contents

1 X-ray diffraction

X-ray diffraction patterns were collected on a ground single crystal of $PdPb_2$, and refinements were performed, as shown below in **Figure 1**.

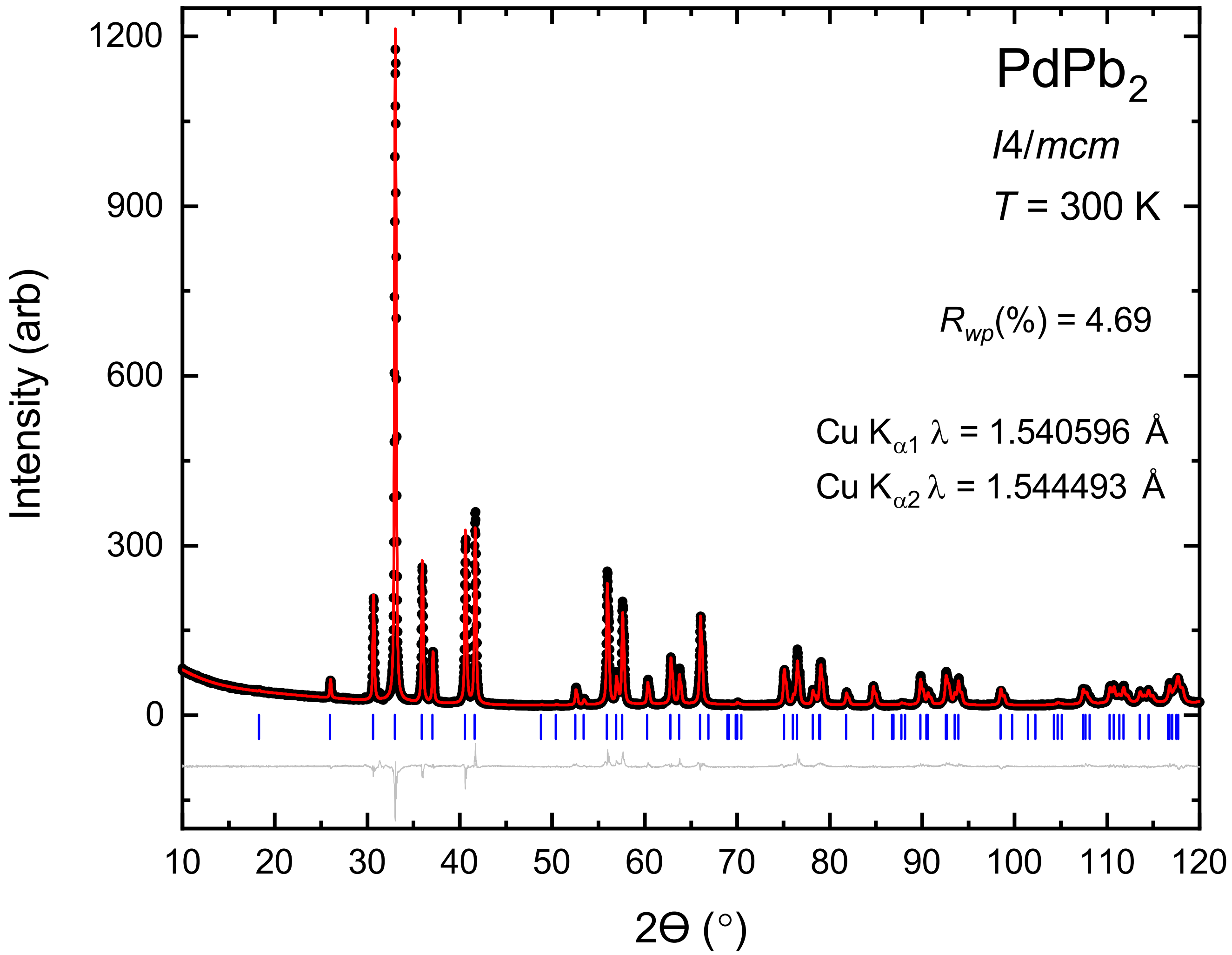

Figure 1. Laboratory X-ray diffraction pattern of PdPb$_2$, with data shown as black points and a fit to the $I4/mcm$ literature structure shown as a red line[1]. Measurements down to $T = 20$ K (not shown) show no signs of a structural phase transition down to that temperature.

2 Laue X-ray diffraction

The Laue patterns for oriented single crystals of PdPb$_2$ are shown in **Figure 2** (110) and **Figure 3** (001). Both crystals were cut from the same grown induction furnace crystal. The surfaces were polished to minimize oxidation. The exposed crystal directions are within 2% tilt.

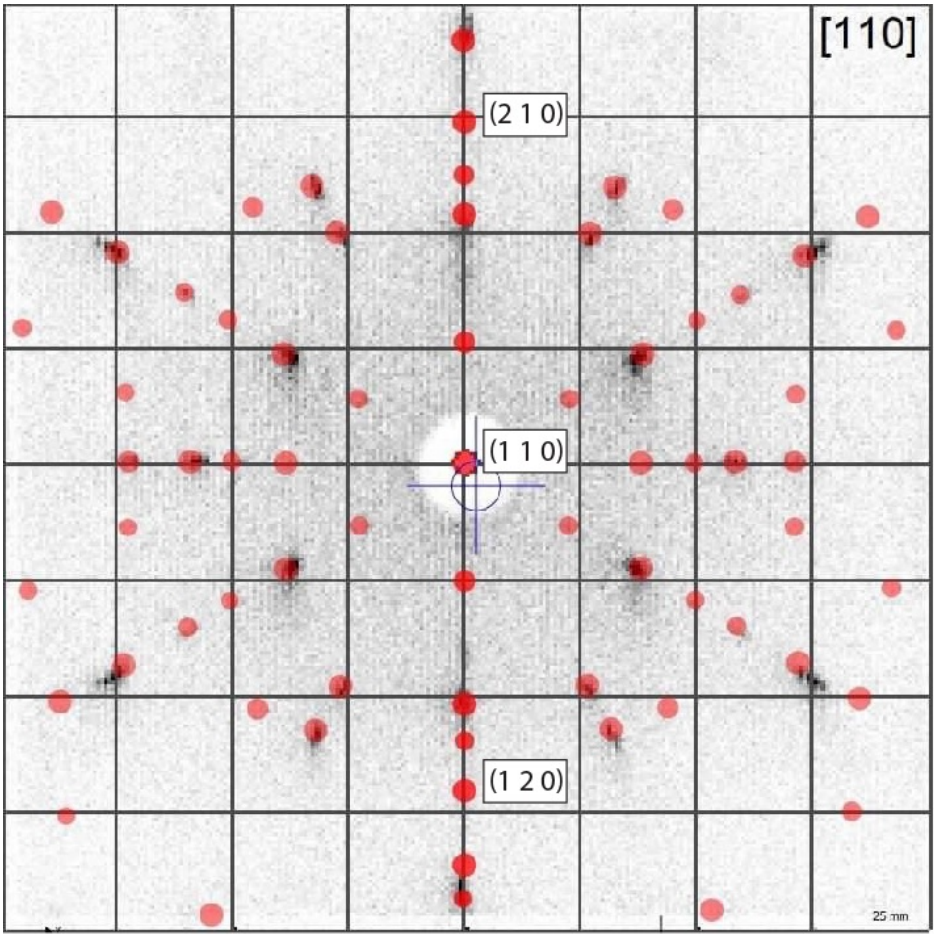

Figure 2. Laue diffraction pattern image of $PdPb_2$. The sample has been aligned in the [110] direction.

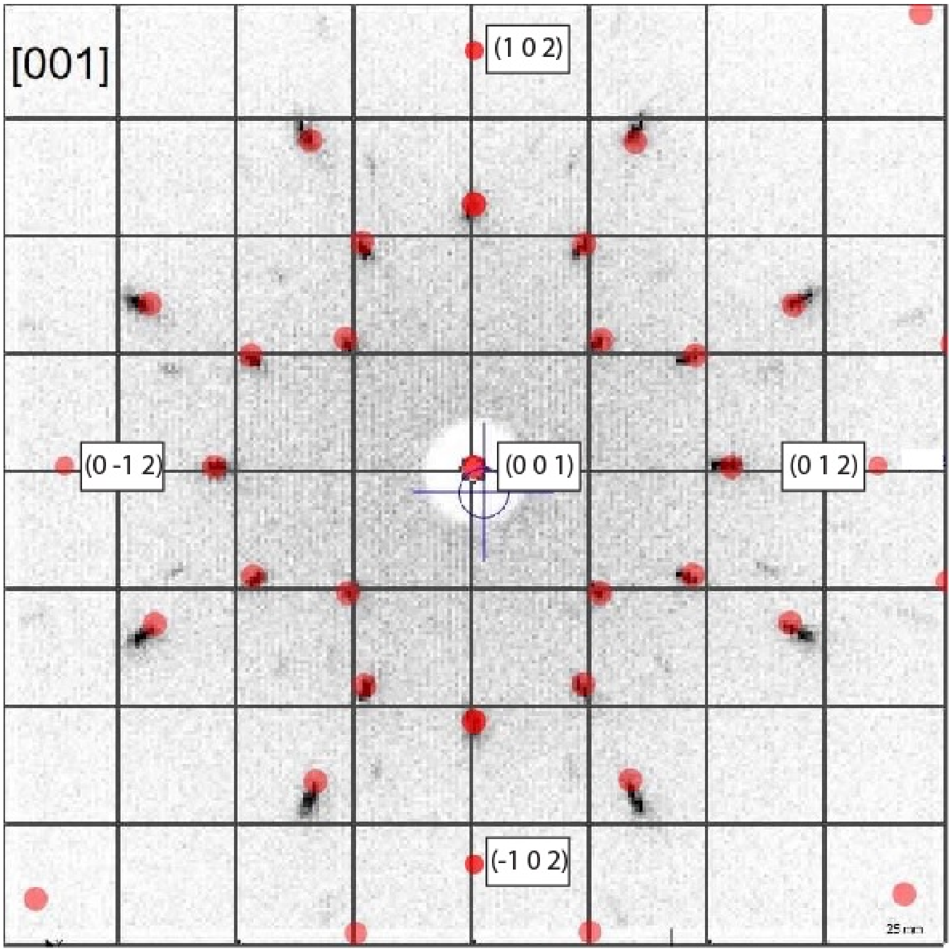

Figure 3. Laue diffraction pattern image of $PdPb_2$. The sample has been aligned in the [001] direction.

3 Micro-computed tomography

X-ray μCT measurements were performed on crystals to both determine whether macroscopic inclusions were present and to accurately assess the volume of crystals used in measurements of microwave perturbation and magnetization. No macroscopic inclusions were detected, as shown in **Figure 4**. A video of the scan can be found at [link].

The determined volumes of the crystals used for magnetization were 0.006584(2) cm^{-3} for the 110 oriented crystal, and 0.005924 (1) cm^{-3} for the 001 oriented crystal. The volume of the sample used in microwave cavity perturbation measurements was 0.000588(2) cm^{-3}.

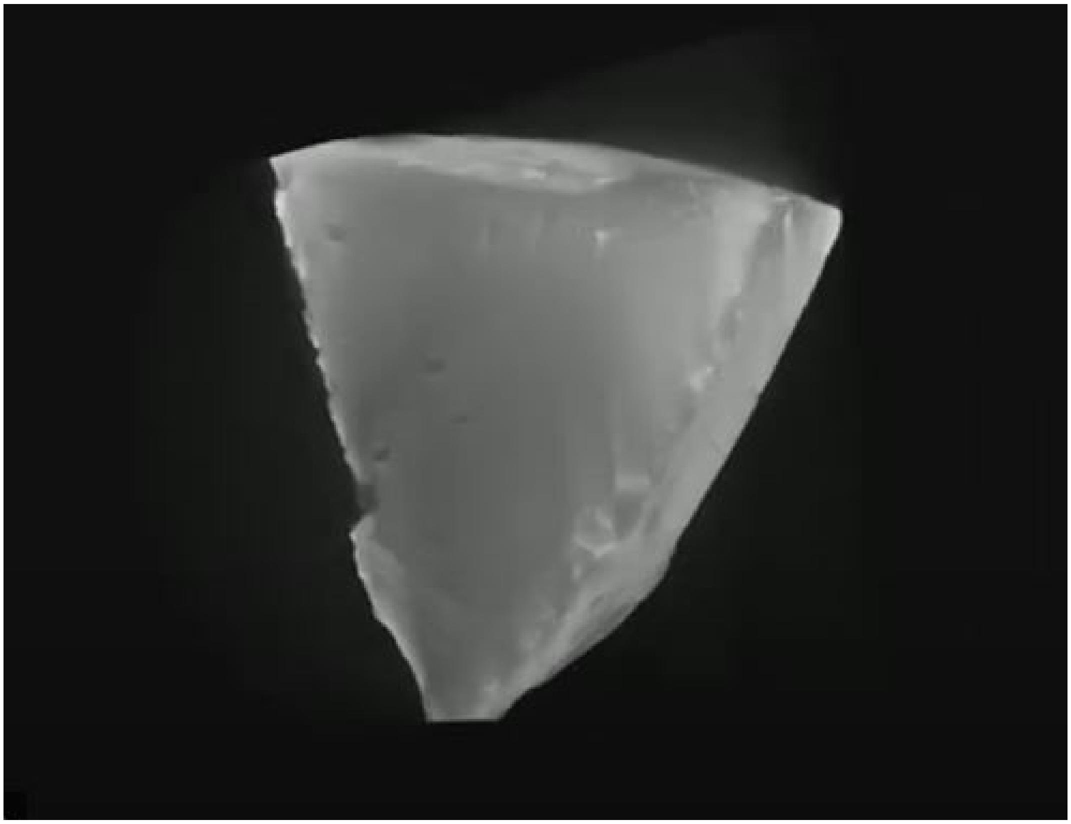

Figure 4. A micro-computed tomography analysis was carried out on a small piece of $PdPb_2$ single crystal. This is the sample that was measured using heat capacity. A video can be found at [link]. No large-scale inclusions can be seen, nor secondary phases by differences in contrast

.

4 Sample demagnetization and lower critical field

The lower critical field H_{c1}^* of two crystals of $PdPb_2$, with the applied field parallel to the 110 and 001 directions, was determined after accounting for demagnetization due to the geometry of the samples measured. This was performed by fitting the linear portion of the $M(H)$ curves at varying tempertures to $M_{fit} = a\mu_0 H + b$, where the slope a is related to the sample demagnetization factor N by $-a = 1/4\pi(1-N)$. For the 110 aligned sample, $N = 0.6182$. For the 001 aligned sample, $N = 0.6211$.

The lower critical field H_{c1}^* was then determined by subtracting the linear portion of the $M(H)$ curves and then determining the field at which a deviation occurred, as shown in **Figure 5**.

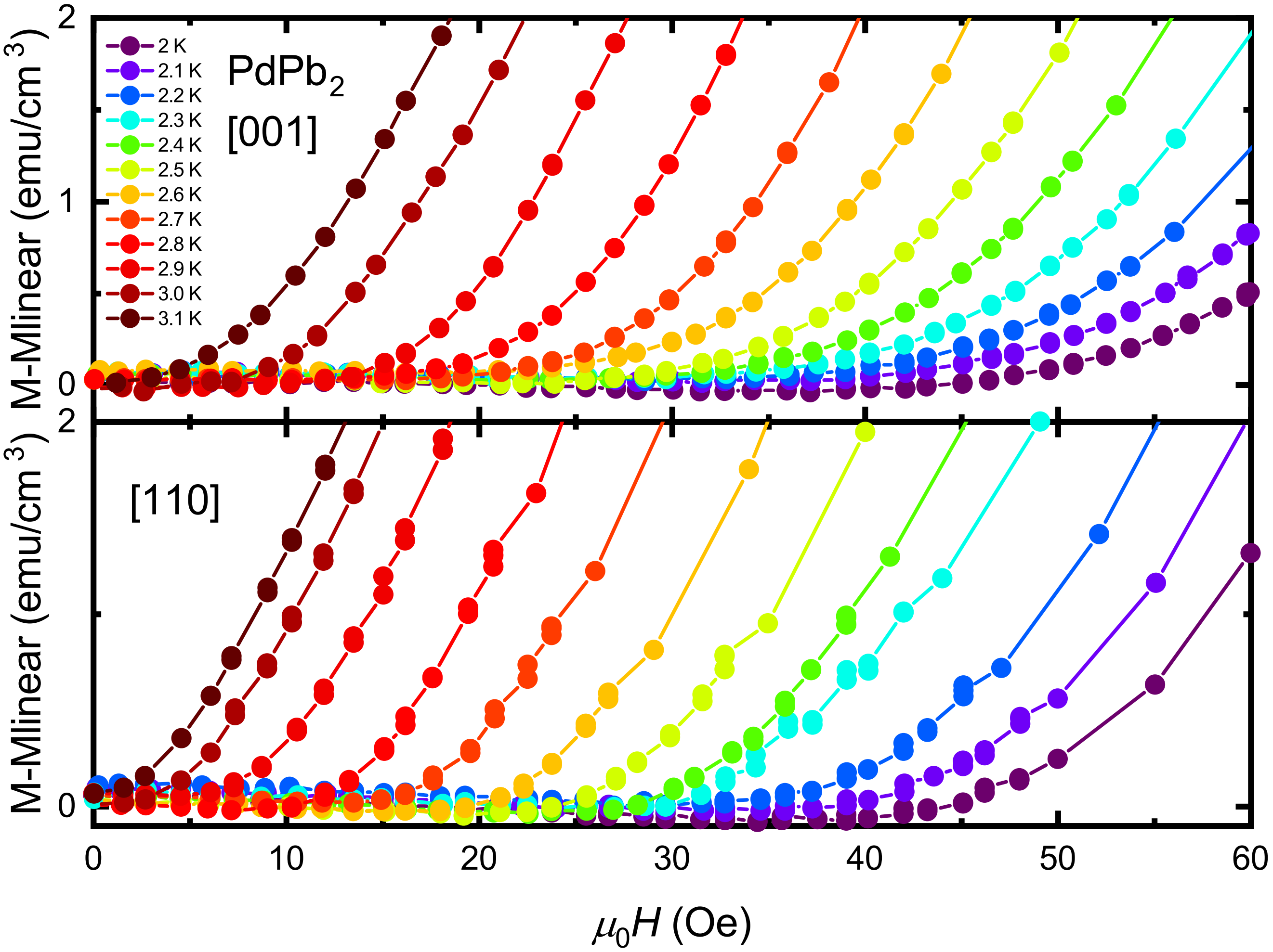

Figure 5. Magnetization plots of a $PdPb_2$ crystal aligned along two crystallographic directions, [110] and [001]. Demagnetization effects due to sample geometry were taken into account, and the zero-field cooled (ZFC) curve for either direction shows that the superconducting volume fraction is at least 97% for the sample

.

5 Zero-field cooled vs. field-cooled magnetization: superconducting volume fraction

Temperature dependent susceptibility data is shown in **Figure 6** for 110 and 001 aligned crystals of $PdPb_2$. Sample demagnetization was accounted for as aforementioned, using the same values. Our data indicates that 99.1(2)% of the volume of the 110 aligned sample is superconducting, whereas 97.7(1)% of the 001 aligned sample is. The error arises from the measurement error in the volume susceptibility χ_V.

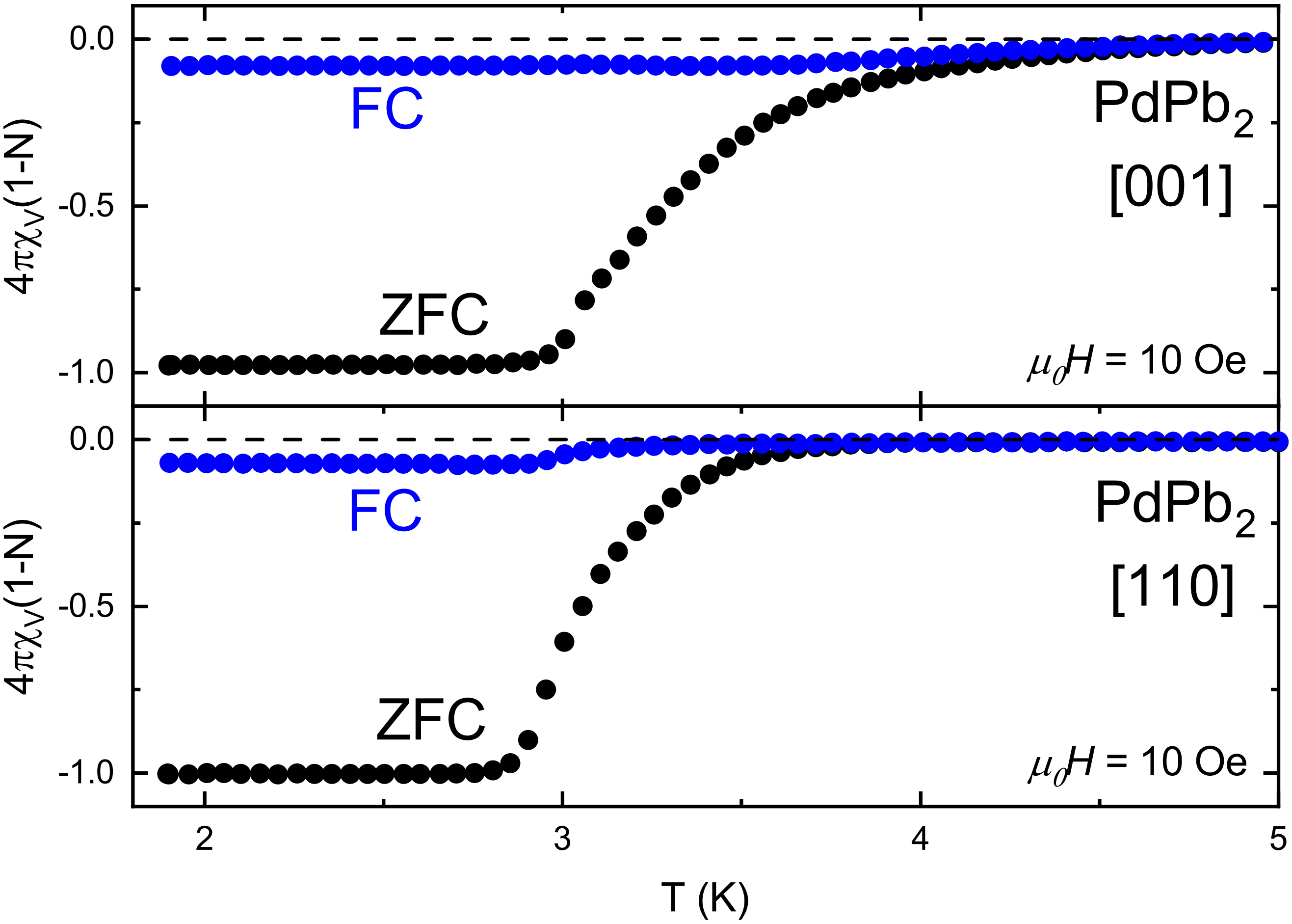

Figure 6. Magnetization plots of a PdPb$_2$ crystal aligned along two crystallographic directions, [110] and [001]. Demagnetization effects due to sample geometry were taken into account, and the zero-field cooled (ZFC) curve for either direction shows that the superconducting volume fraction is at least 97% for the sample
.

6 Analysis of high temperature heat capacity

To justify our use of a higher order β_5 phonon term in the low temperature heat capacity, measurements of heat capacity were performed up to $T = 100$ K. The presence of an Einstein mode with $T_E = 49.5(4)$ K is evident, as shown in **Figure 7** as a C/T^3 vs T plot.

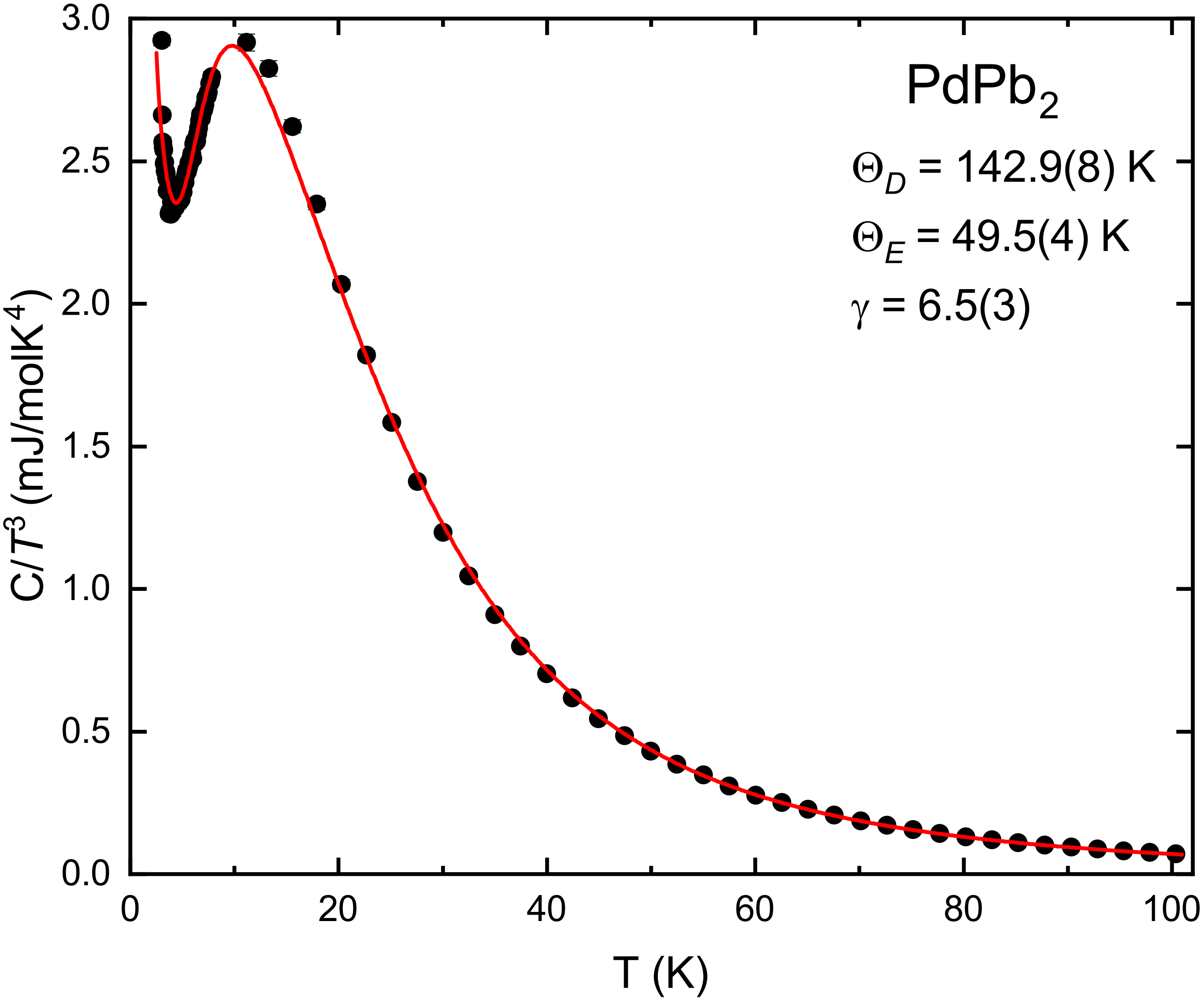

Figure 7. Heat capacity over temperature cubed, highlighting the Einstein mode that is present at low temperature.

.

The fit shown is to the following equation:

$$\frac{C_P}{T^3} = \frac{E(\Theta_E,T)}{T^3} + \frac{D(\Theta_D,T)}{T^3} + \frac{\gamma}{T^2}$$

where the Einstein contribution $E(\Theta_E,T)$ is given by:

$$E(\Theta_E,T) = 3s_E R(\Theta_E/T)^2 \frac{\exp(\Theta_E/T)}{[\exp((\Theta_E)/T)-1]^2}$$

and the Debye contribution $D(\Theta_D,T)$ is given by:

$$D(\Theta_D,T) = 9s_D R(T/\Theta_D)^3 \int_0^{\frac{\Theta_D}{T}} \frac{(\Theta_D/T)^4 \exp(\Theta_D/T)}{[\exp(\Theta_D/T)-1]^2} d\frac{\Theta_D}{T}$$

Here, s is the oscillator strength, R is the molar Boltzmann constant, and Θ_D and $Theta_E$ are the Debye and Einstein temperatures, respectively. The final fit parameters are $s_E = 0.21(1)$, $s_D = 2.86(2)$, $\Theta_D = 142.9(8)$ K, and $\Theta_E = 49.5(6)$ K. The total number of oscillators adds up to $s_tot = 3.07(9)$, in agreement with the total number of atoms per formula unit.

7 Derivations of superconducting parameters

Based on measurements of heat capacity, resistivity, and magnetization, the superconducting parameters in the main paper were obtained in the following way.

The lower critical field H_{c1}^{*} for each crystallographic orientation was obtained by first subtracting off the linear portions of the M(H) curves, then taking the points where the magnetization started to be non-zero. This was done after accounting for demagnetization effects, as previously discussed, thus resulting in H_{c1}^{*}.

The upper critical field H_{c2} for each crystallographic orientation was determined by taking the greatest linear slope of each $\rho(T)$ curve under discrete magnetic fields, and taking the x-intercept of each line.

Based on the values of H_{c1}^{*} and H_{c2}, the values for the penetration depth $\lambda(T=0)$ and coherence length $\xi(T=0)$ were determined. The coherence length was determined by:

$$H_{c2} = \Phi_0/2\pi\xi(0)^2$$

This value was then used along with the lower critical field values to determine the penetration depth via:

$$H_{c1}^{*} = \Phi_0/4\pi\lambda(0)^2 \ln\lambda(0)/\xi(0) + \alpha$$

Where α is a mathematical parameter defined as:

$$\alpha = 1/2 + (1+\ln 2)/(2\kappa - \sqrt{2} + 2)$$

Given these two values, the derived Ginzburg-Landau parameter κ was derived via:

$$\kappa = \frac{\lambda(0)}{\xi(0)}$$

Lastly, the thermodynamic critical field H_c was calculated by:

$$H_{c1}^{*} H_{c2} = H_c \ln\kappa$$

8 Scanning electron microscopy and energy dispersive spectroscopy

Two SEM images are shown for $PdPb_2$ in **Figure 8 A**, as well as EDS maps at two different length scales. These length scales are relatively large (0.5 mm (**B**) and 0.05 mm (**C**)), though no macroscopic structure is observed in either Pd or Pb content. The sample appears to be fully homogenous. Despite observations of excess Pb through a higher-than-3.0 K T_c in resistivity and magnetization, there appear to be no density fluctuations in EDS scans targeting Pb at either length scale. It is possible that this occurs at lower length scales. Further, there appear to be no inclusions of other elements, nor do there appear to be Pd or Pb rich/deficient phases.

The samples were also polished right before inserting them into the SEM instrument to minimize surface oxidation. By doing so rapidly, nearly all surface oxidation is avoided. Samples with heavy surface oxidation (exposed to air for greater than 24 hours) were also measured, and showed Pd-Pb-O ratios consistent with the presence of PbO and $PdPbO_2$ on the surface, both of which are non-metallic.

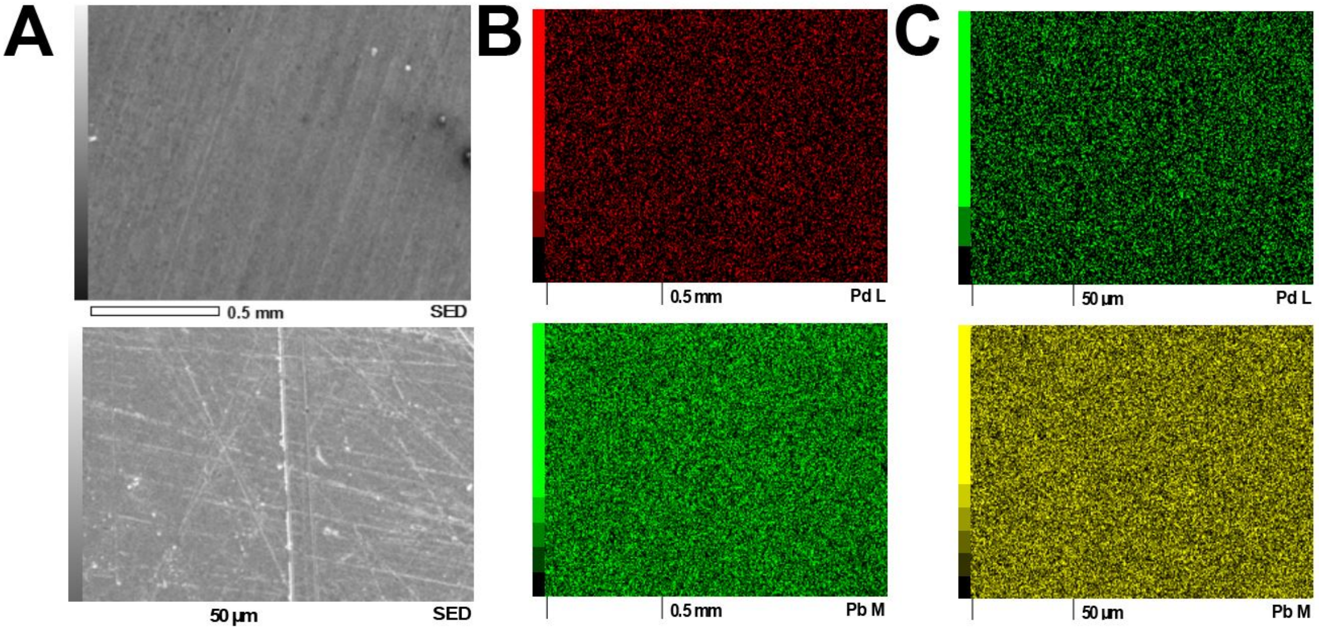

Figure 8. SEM and EDS maps of a [110] oriented crystal of $PdPb_2$. **A** shows direct images of the surfaces. The crystal was polished using sand paper before the measurement, leading to mesoscopic scratches on the surface. **B** and **C** show energy-dispersive spectroscopic maps at the mm and μm scale, showing no signs of any secondary phases or areas of non-stoichiometry within these length scales. Scans were run for one hour each.

Table 1. Table of sample values extracted from EDS.

Formula	Mass%	Atom%	Sigma	Net	K Ratio	Line
Pd	20.52	33.42	0.13	64470	0.0018304	L
Pb	79.58	66.58	0.22	351540	0.0086860	M

9 Microwave cavity perturbation technique measurement procedure

The microwave cavity perturbation technique (MCPT) was used to resonantly measure the microwave complex surface impedance of the $PdPb_2$ single crystals. The sample was mounted using N-grease on an insulating sapphire rod in a superconducting right-circular cylindrical cavity resonator made of NbTi, $T_c \sim 10$ K, designed to resonate on the TE_{011} mode at resonant frequency of $\omega_0 \approx 18.66$ GHz. Before measuring the sample itself, the empty cavity resonant frequency, ω_0, and bandwidth of the resonance, Γ_0, as a function of temperature were measured. The bandwidth is related to quality factor of the cavity Q through the relation $Q = \omega_0/\Gamma$, and the quality factor for our cavity is $\sim 10^6$ in the superconducting state. Upon the insertion of the $PdPb_2$ sample into the cavity, the change in resonant frequency, $\Delta\omega(T) = \omega_s(T) - \omega_0(T)$, and the bandwidth $\Delta\Gamma(T) = \Gamma_s(T) - \Gamma_0$ was measured for temperature ranging from 0.5 K to 5 K. Assuming all external conditions were kept constant during both measurements, external contributions to the Γ from cables and coupling would ideally be removed. Sample heating was minimized by using a low microwave power of -20 dBm.

The technique relies on the fact that the introduction of the sample is a small perturbation on the overall structure of the electromagnetic standing wave pattern within the cavity and is therefore adiabatic. Thus, a $PdPb_2$ crystal of ~ 3 mg ($\sim 6.8 \times 10^{-4}$ cm^{-3}) was placed in the cavity of volume 9.26 cm^{-3}. For the measurement, the sample was placed at the magnetic field antinode of TE_{011} mode of the cavity, see **Figure 9**. This results in the measured frequency shift to contain components of both the electric and magnetic responses of the sample. This results in the measured frequency shift to contain components of both the electric and magnetic responses of the sample. Thus, the measured resonant properties can be related to generalized electromagnetic susceptibility[2,3]. In the skin-depth regime applicable only to samples with large conductivities, such as superconductors, where the microwaves are confined close to the sample surface the measured resonant properties, $\Delta\omega \approxeq \Delta\omega + i\Delta\Gamma/2$, can be related to complex surface impedance, $\tilde{Z}_s = R_s + i\Delta X_s$, through the equation $\frac{\Delta\tilde{\omega}}{\omega_0} = \xi\tilde{Z}_s + \lim_{|\tilde{\sigma}|\to\infty}\frac{\Delta\tilde{\omega}}{\omega_0}$ where constants ξ and $\lim_{|\tilde{\sigma}|\to\infty}\frac{\Delta\tilde{\omega}}{\omega_0}$ are known as the resonator constant and metallic shift respectively, both of which depend on the mode of resonance, the sample geometry, and the sample position within the cavity. Physically, the metallic shift corresponds to the shift in the complex frequency of the sample if it was infinitely conducting. The resonator constant ξ accounts for the size of electromagnetic field at the sample position. These quantities are calibrated from the normal state resistivity of the sample. The real part of complex surface impedance, R_s is the surface resistance, and the imaginary part ΔX_s is the change in surface reactance.

The sample geometric factors, metallic shift, and resonator constant, in the expression $\tilde{Z}_s = \frac{1}{\xi}\left(\frac{\Delta\tilde{\omega}}{\omega_0} - \lim_{|\tilde{\sigma}|\to\infty}\frac{\Delta\tilde{\omega}}{\omega_0}\right)$, can either be calculated analytically by solving the field equations inside the resonator cavity or experimentally by comparing the normal state resistivity. For example, if a perfect spherical metallic sample is placed at the magnetic field antinode of the cavity, in the Hagen-Rubens limit ($\omega\tau \ll 1$), the metallic shift is given by $-\gamma_0(V_s/V_c)/(n-1)$ and the resonator constant is given by $-9i\gamma_0(V_s/V_c)\omega_0 Z_0 a/4c_0$, where γ_0 is the mode constant, n is the depolarization factor, ω_0 is the cavity frequency, V_s is the sample volume, V_c is the volume of the cavity and z_0 is the impedance of vacuum[3]. However, the samples used in our measurement are small and not of well defined shape, making it hard to analytically calculate the exact geometric factors in order to accurately determine the metallic shift and the resonator constant.

In the present case, we calculate the value of metallic shift by equating the experimentally obtained $R_s(T) = X_s(T)$ in the normal state. Similarly, one can determine the value of the resonator constant ξ by comparing the experimentally measured R_s with the calculated $R_s = \sqrt{\mu\omega\rho_{dc}/2}$ from electrical resistivity ρ_{dc} of a dc transport measurement in the normal state or by directly equating the microwave conductivity in the normal state with the dc conductivity from a transport measurement. This equality is expected for good metals in Hagen-Rubens limit ($\omega\tau \ll 1$), where the scattering rate is much higher than the measurement frequency ($1/\tau \gg \omega$), so the conductivity of the sample (described by the Drude model: $\tilde{\sigma} = ne^2\tau/m^*(1+i\omega\tau)$) has only a real part to a good approximation[3]. We can obtain the scattering rate in the normal state by comparing the conductivity to the Drude model, $i\omega\mu/\tilde{Z}_s = ne^2\tau/m^*(1+i\omega\tau)$. This equation can be solved by considering the real and the imaginary parts individually as the two equations with ne^2/m^* and τ as two variables. We find the Oscillator strength $ne^2/m^* = 1.53\times10^{29}$ $\mathrm{C^2m^{-3}kg^{-1}}$ and $\omega\tau \leq 0.04 \ll 1$.

10 Deriving effective surface impedance in terms of layers

For a thin film normal fluid with conductivity σ and thickness t backed by a bulk superconducting material with an impedance Z_{sc}, A. R. Kerr has derived the expression for the effective impedance[4],

$$Z_{\text{eff}} = \frac{k}{\sigma}\left[\frac{e^{kt} + \frac{\sigma Z_{sc}-k}{\sigma Z_{sc}+k}e^{-kt}}{e^{kt} - \frac{\sigma Z_{sc}-k}{\sigma Z_{sc}+k}e^{-kt}}\right]$$

Here, the wave vector for normal fluid channel is given by $k(\sigma) = \frac{1+i}{\delta(\sigma)}$ and the classic skin depth is $\delta = \left(\frac{2}{\omega\sigma\mu}\right)^{1/2}$. Assuming $kt = x$, $\frac{\sigma Z_{sc}-k}{\sigma Z_{sc}+k} = a$ and take $e^x = 1+x$ (for small x). Thus:

$$Z_{\text{eff}} = \frac{k}{\sigma}\left[\frac{e^x + ae^{-x}}{e^x - ae^{-x}}\right] = \frac{k}{\sigma}\left[\frac{(1+a)+(1-a)x}{(1-a)+(1+a)x}\right]$$

$$= \frac{k}{\sigma}\left[\frac{\sigma Z_{sc} + kx}{k + \sigma Z_{sc}x}\right]$$

$$= \frac{k}{\sigma}\left[\frac{\sigma Z_{sc} + k(kt)}{k + \sigma Z_{sc}(kt)}\right]$$

$$Z_{\text{eff}} = \frac{\frac{Z_{sc}}{\sigma t} + (\frac{k}{\sigma})^2}{\frac{1}{\sigma t} + Z_{sc}}$$

Ignoring higher order terms and taking normal impedance $1/\sigma t = R_t$ we get,

$$Z_{\text{eff}} \approx \frac{Z_{sc}R_t}{Z_{sc}+R_t}$$

At low temperatures $T < T_c/3$, the bulk superconductor should have a purely imaginary impedance e.g. $Z_{sc} = iX_{sc}$. This implies that

$$R_s + iX_s = \frac{R_t iX_{sc}}{R_t + iX_{sc}},$$

$$R_t = \frac{R_s^2 + X_s^2}{X_s}.$$

These expressions are used to extract R_t in the main text.

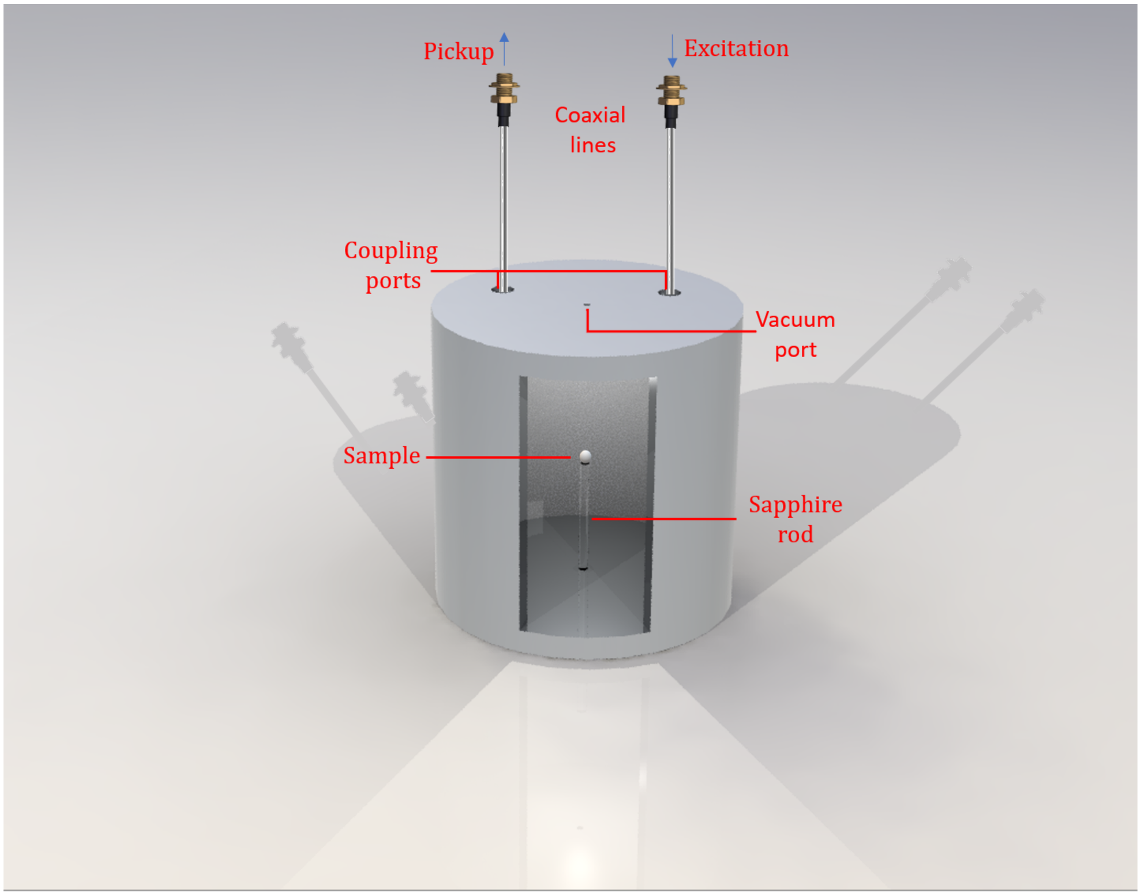

Figure 9. Schematic of our cavity resonator. A cut away on the front is included so that the sapphire rod, used to mount a sample, is visible. The top plate contains holes for inserting coaxial cables with small antenna to couple to the cavity. These coupling ports are located at the magnetic field maximums of the TE_{011} mode.

11 Penetration depth

One of the important properties one can extract from the complex conductivity is the effective penetration depth. For a conventional superconductor, in the superconducting state for $T \to 0$, $\sigma_1 \ll \sigma_2$ implies $R_s + iX_s = i\sqrt{\mu_0\omega/\sigma_2}$. In the case of $R_s \ll X_s$, taking $\sigma_2 = 1/\mu_0\omega\lambda^2$, we obtain $X_s = \mu_0\omega\lambda$. Thus, the temperature-dependent penetration depth $\lambda(T)$ is directly proportional to the sample's reactance, as $X_s(T) = \mu_0\omega\lambda(T)$, where μ_0 s the permeability of free space and ω is the microwave resonance frequency. In our case $\sigma_2(T \to 0)/\sigma_1(T \to 0) \sim 10$, so the condition $\sigma_1 \ll \sigma_2$ is satisfied weakly as compared to a convetional superconductor where $\sigma_1(0)/\sigma_2(0) = 0$. We take our extracted penetration depth as a good approximation of the actual penetration depth. The superconducting gap magnitude can further be extracted at temperatures $T_c/T \geq 3$ by fitting to $\lambda(T)$ using the following:

$$\Delta\lambda(T) = \lambda(0)\sqrt{\frac{\pi\Delta(0)}{2k_BT}}exp\left(-\frac{\Delta(0)}{k_BT}\right)$$

where $\lambda(0)$ is the penetration depth at $T = 0$ K and k_B is the Boltzmann constant. The superconducting gap is found to be $\Delta(0) \approx 0.4$ meV, which is in good agreement with the superconducting energy gap extracted from heat capacity measurement.

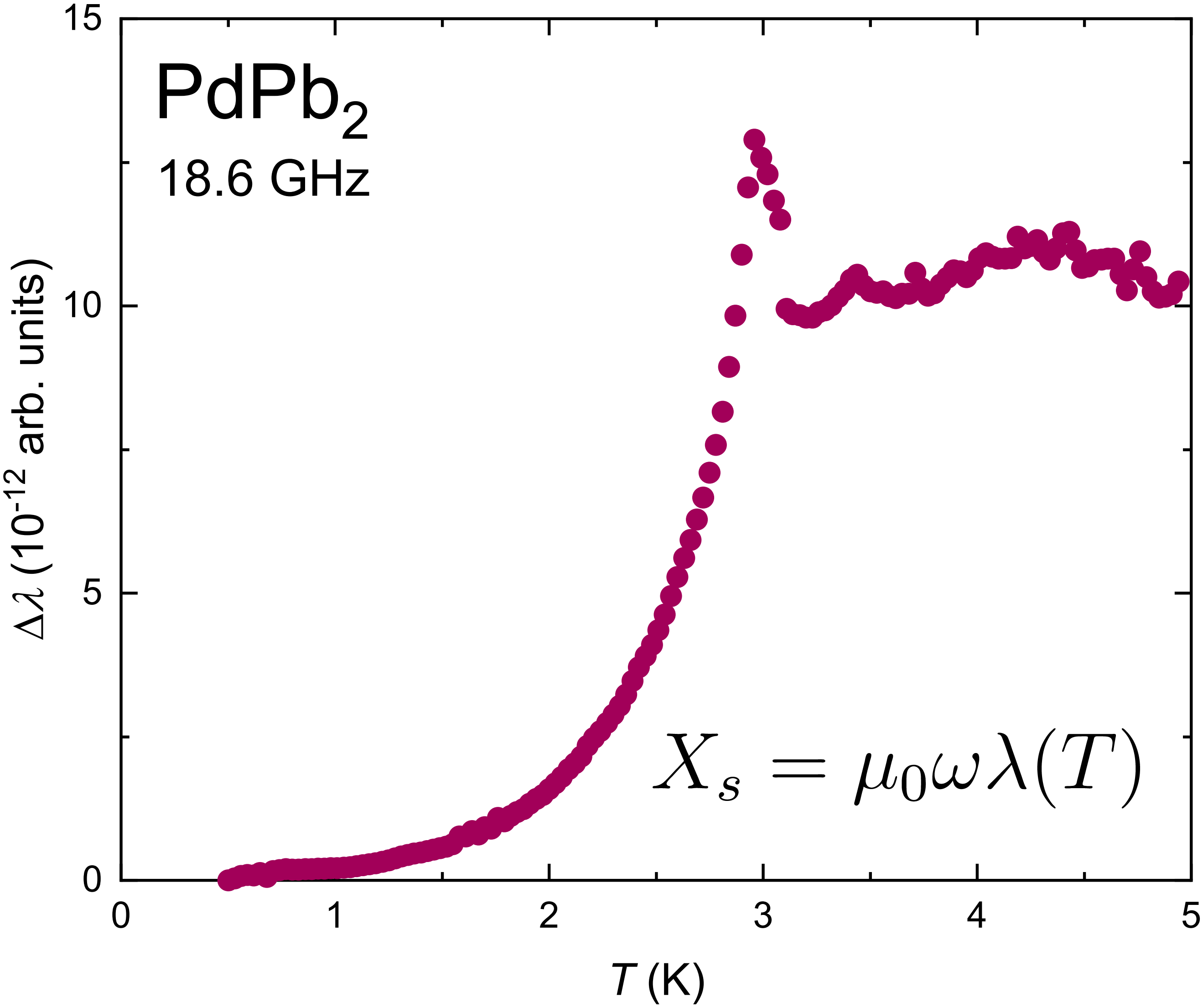

Figure 10. The change in penetration depth as a function of temperature is extracted from the surface reactance X_s for $PdPb_2$.

References

1. Havinga, E., Damsma, H. & Hokkeling, P. Compounds and pseudo-binary alloys with the CuAl2(c16)-type structure i. preparation and x-ray results. *J. Less Common Met.* **27**, 169–186, DOI: 10.1016/0022-5088(72)90028-8 (1972).
2. Laurita, N. J. *Low Energy Electrodynamics Of Quantum Magnets*. Ph.D. thesis (2017).
3. Dressel, M., Klein, O., Donovan, S. & Grüner, G. Microwave cavity perturbation technique: part III: applications. *Int. J. Infrared Millim. Waves* **14**, 2489–2517 (1993).
4. Kerr, A. R. Surface impedance of superconductors and normal conductors in em simulators. *Natl. Radio Astron. Obs. Interal Rep.* **302** (1996).